ARTICLES

Scaling in three-dimensional and quasi-two-dimensional rotating turbulent flows

Charles N. Baroud,[a] Brendan B. Plapp, and Harry L. Swinney[b]
Center for Nonlinear Dynamics and Department of Physics, The University of Texas at Austin, Austin, Texas 78712

Zhen-Su She
State Key Lab for Turbulence and Complex Systems and Department of Mechanics and Engineering Science, Peking University, Beijing 100871, People's Republic of China and Department of Mathematics, University of California at Los Angeles, Los Angeles, California 90095

(Received 5 June 2002; accepted 2 April 2003; published 11 June 2003)

We have made velocity time series measurements (using hot film probes) and velocity field measurements (using particle image velocimetry) on turbulent flow in a rotating annulus. For low annulus rotation rates the Rossby number was of order unity and the flow was three-dimensional (3D), but at high rotation rates the Rossby number was only about 0.1, comparable to the value for oceans and the atmosphere on large length scales. The low Rossby number (quasi-geostrophic) flow was nearly two-dimensional (2D), as expected from the Taylor–Proudman theorem. For the 3D flow we found that the probability distribution function (PDF) for velocity differences along the direction of the flow, $\delta v(d)=v(x_0+d)-v(x_0)$, was Gaussian for large separations d and non-Gaussian (with exponential tails) for small d, as has been found for nonrotating turbulent flows. However, for low Rossby number flow, the PDF was self-similar (independent of d) and non-Gaussian. The exponents characterizing the structure functions, $S_p=\langle(\delta v)^p\rangle\sim d^{\zeta_p}$ were obtained by the extended self-similarity method. For 3D flow the exponents departed from $p/3$ with increasing p, as has been found for turbulence in nonrotating flows, while for the quasi-2D turbulent flow, the exponents increased linearly with p, as expected for a self-similar flow. We applied the β-test of the hierarchical structure model [She and Lévêque, Phys. Rev. Lett. **72**, 336 (1994)] and found that β remained constant at $\beta\simeq 0.75$ as the rotation was increased from the 3D to the 2D regime; this indicates that both the quasi-2D and 3D flows are highly intermittent. The PIV images provided another indication of the intermittency—both the quasi-2D and 3D flows had coherent vortices which could be distinguished from the background flow. We also applied the γ-test of the hierarchical structure model and found that γ increased from 0.18 for the 3D flow to 0.34 for the quasi-2D flow; the latter value is in accord with expectation for self-similar turbulence. We conclude that our rotating 3D flow is similar to nonrotating turbulent flows, while the rotating quasi-2D turbulence is different from both the 3D rotating turbulence and from nonrotating 2D turbulence studied in other experiments. © *2003 American Institute of Physics.* [DOI: 10.1063/1.1577120]

I. INTRODUCTION

Our study uses rotation to two-dimensionalize a turbulent flow, in contrast with most other recent laboratory studies of two-dimensional (2D) turbulence, where two dimensionality has been approximated using thin liquid layers.[1,2] If a volume of fluid is rotated rapidly, the derivatives of velocity in the axial direction become small by the Taylor–Proudman theorem; the resultant quasi-two-dimensionality persists even for strongly turbulent rapidly rotating flows.[3] A dimensionless number that provides a measure of the degree of two dimensionality is the Rossby number Ro, which compares inertial effects to Coriolis effects: The velocity field becomes strictly 2D in the limit $Ro\to 0$. At the highest rotation rates of the present experiment, $Ro\simeq 0.1$, sufficiently low so that the flow is essentially 2D. A flow with sufficiently rapid rotation and low dissipation is called a quasi-geostrophic flow;[4] for brevity, we refer to it simply as 2D.

Our study is the first to determine the statistical properties of low Rossby number turbulence.[5] Further, by decreasing the rotation rate, we examine the transition from 2D to 3D turbulence. The measurements of statistical properties of these turbulent flows and the visualization of the velocity and vorticity fields provide new insight into the relationship be-

[a]Present address: Laboratoire d'Hydrodynamique (LadHyX), Ecole Polytechnique, 91128 Palaiseau, France. Electronic mail: baroud@ladhyx.polytechnique.fr
[b]Electronic mail: swinney@chaos.ph.utexas.edu

tween intermittent structures in the flow and the scale dependence of the statistics.

Stretching and folding of vortex tubes is a fundamental process in 3D turbulence that is not allowed in 2D flows. In 3D turbulence, vortices stretch and fold repeatedly until they eventually collapse to intense filaments.[6] These filaments affect the transfer in the energy cascade, creating a rate of transfer that exhibits strong scale-dependence. Velocity measurements with a fixed probe yield intermittent bursts corresponding to vortex filaments sweeping by the probe, and this intermittency is an important characteristic property of 3D turbulence.[6] In two dimensions, the vortex tubes cannot stretch axially and fold, but numerical simulations of 2D turbulence (see, e.g., Kevlahan and Farge[7]) have found that energetic coherent vortices can become deformed and fold in the plane of the flow; they then form a ''turbulent background'' which surrounds the remaining coherent structures.[6] Thus 2D flows can exhibit a kind of intermittency through the switching between the large coherent structures and the small scale turbulence, even though the 3D mechanism of stretching and folding is not present.

A standard test for intermittency is to examine the scaling of the structure functions, which are moments of the velocity increments.[6,8] The pth-order longitudinal structure function is defined as

$$S_p(d)=\langle[v(x_0+d)-v(x_0)]^p\rangle, \tag{1}$$

where d is the separation distance between two points and v is the velocity component in the direction of d. Kolmogorov's 1941 theory (K41), assuming self-similar statistics, predicts that the pth moment of the velocity increments should be proportional to d^{ζ_p}, where $\zeta_p=p/3$. Measurements of ζ_p in 3D turbulence experiments and simulations have shown a nonlinear dependence on p (see Ref. 8 and references therein), indicating scale-dependent rather than self-similar statistics.

Numerical simulations[9] of 2D turbulence yield $\zeta_p=p/3$ (see also Refs. 10 and 11). However, two-dimensional turbulence is difficult to produce in the laboratory. Paret and Tabeling[1] studied quasi-two-dimensional turbulence in a thin layer of electrolyte (driven by a current and perturbed magnetically), and they obtained $\zeta_p=p/3$. Their probability distribution functions (PDFs) of velocity differences were nearly Gaussian over the whole inverse cascade range. Experiments in gravitationally driven soap films[2,12] observed pronounced departures from the $p/3$ prediction, and the velocity difference PDFs shifted from exponential at small separations to Gaussian at large separations.[2]

Recently, we found that turbulence in our rotating system exhibits, for sufficiently rapid rotation, a scaling different from K41: Although ζ_p varied linearly with p, the exponent was found to be $\zeta_p=p/2$ rather than $\zeta_p=p/3$.[5] The corresponding energy spectrum was $E(k)\sim k^{-2}$, consistent with the predictions for 2D Lundgren spiral vortices[13] and with the predictions for rotating turbulent flows.[14,15] These results indicated that the quasi-2D turbulence in rapidly rotating system is different from turbulence in 2D nonrotating systems.

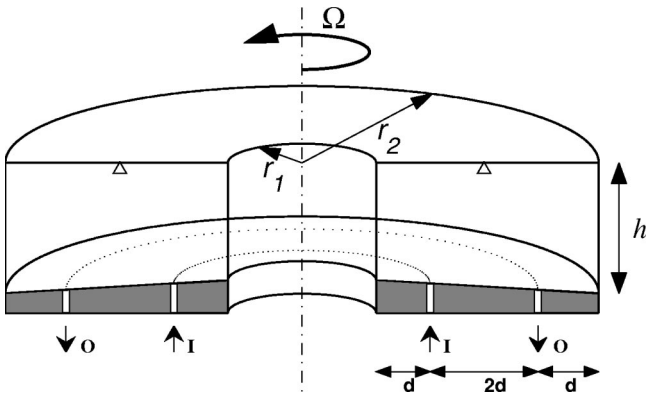

FIG. 1. Cutaway of rotating annulus. $r_1=10.8$ cm, $r_2=43.2$ cm, $d=8.1$ cm, $h=17.8$ at r_1 and $h=20.3$ cm at r_2. I is the inflow, and O is the outflow. The locations of the two hot-film probes are marked △.

Here we test for intermittency in rotating flows not only by examining the structure function scaling but also by applying the β- and γ-tests of the Hierarchical Structure model.[17] This model involves a hierarchy of functions $F_p(d)=S_{p+1}(d)/S_p(d)$, where the higher intensity fluctuations are described by higher order p of the structure function ratio F_p. The function F_∞ describes the most intermittent, highest intensity fluctuations, assumed to consist of collapsed vortex filaments.[17] The model proposes the existence of a hierarchical symmetry where the functions F_{p+1} can be related to F_p by a power law scaling. If such a scaling exists, the exponent β $(0\leqslant\beta\leqslant1)$ provides a measure of intermittency in the flow: $\beta=1$ corresponds to nonintermittent flow and $\beta=0$ is the opposite extreme. Experiments on Couette–Taylor turbulence[18] and free jets[19] gave similar β values, $\beta=0.83$ and 0.87, respectively.

The other parameter obtained from the Hierarchical Structure model is γ, which provides a measure of how ''singular'' the most intermittent structures are. Hence, a flow where the most intermittent structures are independent of scale d would have $\gamma=0$, which is the case for a one-dimensional collapsed vortex singularity or a shock, while a nonintermittent flow such as Kolmogorov turbulence would have $\gamma=1/3$ (see Sec. V). Couette–Taylor[18] and free jet turbulence[19] both yielded $\gamma=0.10$.

This paper is organized as follows: Section II describes the experiment and the measurements, Sec. III characterizes the flows, including the intermittent structures that we are able to visualize. Section IV presents results for the probability distribution functions of the velocity differences and the structure function exponents. Finally, the β- and γ-tests of the hierarchical structure model are presented in Sec. V, which is followed by a discussion of our results. Appendices A and B describe, respectively, time series analysis techniques and results for the skewness and for the radial dependence of the velocity, vorticity, and shear.

II. EXPERIMENTAL METHODS

Our experimental apparatus consists of an annular tank with a flat rigid lid. The tank can rotate at rates up to $\Omega=20$ rad/s (Fig. 1). An azimuthal jet is generated in the annulus by

pumping water in a closed circuit through two rings of holes at the bottom of the channel. Pumping into the annulus through an inner ring and out through an outer ring produces a net outward flux. This flux couples with the Coriolis force to generate a counter-rotating azimuthal jet. The forcing mechanism is discussed further in Sec. III.

The bottom of the annulus is conical with a constant slope $s=0.1$. In a geophysical context, this beta plane simulates (to first order) the variation of the Coriolis effect due to the curvature of a planet. The sloped bottom also breaks the symmetry between co-rotating and counter-rotating jets. We chose to study the counter-rotating case because a wide, highly turbulent jet forms over a wide range of parameters; in the co-rotating case, the jet is narrower and less turbulent.[20] Another effect of the beta plane is to change the character of the inverse energy cascade at the Rhines wavelength

$$\lambda_\beta=(2U/\beta_R)^{1/2}, \tag{2}$$

where U is a typical velocity, $\beta_R=2s\Omega/h_0$, and h_0 is the mean height. At length scales larger than λ_β, numerical simulations[21] indicate that the inverse energy cascade is quenched, and energy is lost through the radiation of Rossby waves.

The fluid velocity was measured using hot film probes that were inserted into the annulus through the top lid and extended about 1 cm into the fluid. The results discussed below were obtained with the two probes located 180° apart, at radial positions midway between the inner and outer walls of the channel (see Fig. 1). These probes were oriented to measure the azimuthal component of the jet, though they also detected vertical motion without distinguishing the direction. The signal was digitally sampled at 150 Hz for runs lasting two hours, yielding individual data sets of 10^6 points per probe. Measurements were repeated several times to obtain a total of 4×10^6 to 8×10^6 points for each rotation rate and pump rate.

The probes were calibrated before and after each run by first setting the annulus at a constant rotation rate with no pumping, yielding solid-body rotation. A velocity jump of $v=\Omega r_{\text{probes}}$ was produced by suddenly stopping the tank. This process was repeated at several rotation rates, and the data for velocity as a function of voltage were fit with a parabola. The voltage time series from the hot film probes often showed a slow drift over the duration of a run (two hours), but since we were interested in velocity differences over only a few seconds, the effect of this drift was negligible.

The mean velocities from the two simultaneous probes showed a shift (which varied between runs) of a few cm/s from one another. We addressed this problem by off-setting the voltage from one probe until average voltages of the two probes were equal. Then the calibration curve for one probe was used to convert both voltage series into velocities. This procedure produced velocity records for the two probes that had the same means and standard deviations. This method is equivalent to having a hardware DC offset on the acquired voltage, a technique that is commonly used in hot wire anemometry. The same procedure was repeated using the calibration from either probe, and the structure function results were indistinguishable.

The accuracy of the velocity measurements was limited by contaminants in the water, temperature drift, and misalignment of the probes. We reduced these effects by regularly filtering the water, replacing the probes to control for aging and buildup of contaminants (algae), running the probes at a relatively high overheat ($\Delta T\simeq40$ °C), and aligning carefully each probe as it was inserted into the annulus. Our confidence in the data was strengthened by checking the reproducibility for several runs at the same conditions, by comparing simultaneous measurements made with independent probes, and by comparing statistics obtained from the hot film velocity time series with statistics obtained from the instantaneous velocity field measurements described in the following paragraph.

A particle image velocimetry (PIV) system was used to obtain horizontal flow fields near the mid-plane of the annulus. This system consisted of a ring of light emitting diodes (LEDs) that formed a light sheet located at the annulus mid-height. Particles in the light sheet were imaged with a digital camera mounted on a rotating platform located 2 m above the annulus. In the frame of the rotating camera, the annulus was stationary; thus the standard PIV technique could be used to extract the velocity field with respect to the rotating frame.

For each flow condition, 50 instantaneous velocity fields were obtained, equivalent to approximately 2×10^4 velocity values at the radius of the hot film probes. Though this sample size was inadequate for higher order statistics, the spatial information provided by the PIV measurements complemented the long velocity time series obtained with the hot film probes. The spatial resolution of most of the PIV measurements was 0.8 cm, but some measurements, made on a small part of the annulus, had a resolution of 0.3 cm [see Figs. 4(e) and 4(f)].

III. FLOW DESCRIPTION

A. Reynolds and Rossby numbers

Dissipation is small in our flow, i.e., the Ekman friction time, τ_{Ek} (given by $\tau_{Ek}=h_0/2(\nu\Omega)^{1/2}$), typically 80 s, is long compared to the vortex turnover times, typically 0.1–1 s.

Our rotating flow with weak dissipation can be characterized by two dimensionless numbers, the Reynolds number ($Re=UL/\nu$), and the Rossby number ($Ro=\omega/2\Omega$ where ω is the rms vorticity), which is small when Coriolis effects dominate inertial effects. (Alternatively, the Rossby number can be defined as $Ro_g=U/2\Omega L$, but we choose the former definition since it does not require the identification of a length scale L.) Values of the Reynolds and Rossby numbers for the hot film data and some representative PIV data are given in Table I. The Reynolds numbers were obtained with L taken to be the distance between the rings of forcing holes (16.2 cm), U given by the average azimuthal velocity (radial profiles of azimuthal velocity are presented in Appendix B 2), and $\nu=0.01$ cm^2/s.

TABLE I. Conditions for hot film (HF) and some sample PIV measurements (Ref. 22). State I is strongly 2D while state IV is 3D.

	State	Rotation Ω (rad/s)	Pumping Q (cm^2/s)	Re	Ro
HF and PIV	I	11.0	150	2.0×10^4	0.11
	II	6.28	150	1.5×10^4	0.14
	III	3.14	300	2.0×10^4	0.32
	IV	1.57	450	1.4×10^4	0.62
PIV only	V	0.79	550	0.89×10^4	1.1
	VI	0.79	150	0.56×10^4	0.49
	VII	11.0	550	6.8×10^4	0.29

To determine the effect of rotation on the turbulent flow, the Reynolds number was maintained approximately constant (2.0×10^4) as the pumping and rotation rates were varied. This meant that the pumping rate had to be decreased as the rotation rate was increased. To compare our turbulent flow with turbulence in other systems, we computed the Taylor scale Reynolds number, based on the Taylor microscale ($\lambda^{-2}=\langle(\partial_x u)^2\rangle/u_{\rm rms}^2$) and the rms velocity. The value of Re_λ for different flow conditions remained fixed at $Re_\lambda \simeq 360$, with $\lambda_{2D}\simeq 2.0$ cm in the fast rotation case (case I) and $\lambda_{3D}\simeq 1.8$ cm for slow rotation (case IV).

The Rossby number can be interpreted as the ratio of the rotation period of the system ($1/\Omega$) to the typical turnover time of vortices ($1/\omega$). A small Ro indicates a flow where the Coriolis effects are dominant, and the flow is expected to approach a 2D state. The values of the Rossby number for our experiments are plotted in Fig. 2 as a function of rotation and pumping rates. For a fixed pumping rate, the reduction in Ro with increasing rotation rate is clear; the same trend was found for Ro_g, although the actual values depended on the length scale used. Surprisingly, the values of Ro for high-pumping/high-rotation flows are as high as the ones for the low-pumping/low-rotation. This suggests that a lower-energy flow at 1.57 rad/s is as 2D as a high-energy flow at 11 rad/s, which seems unlikely; the structure function exponents indicate that the 11 rad/s flow at high pumping rates is much more two dimensional than the 1.57 rad/s flow at low pumping rate. Thus the relationship between Ro and the two-dimensionality needs to be examined in future experiments and compared with numerical simulations.[15,23]

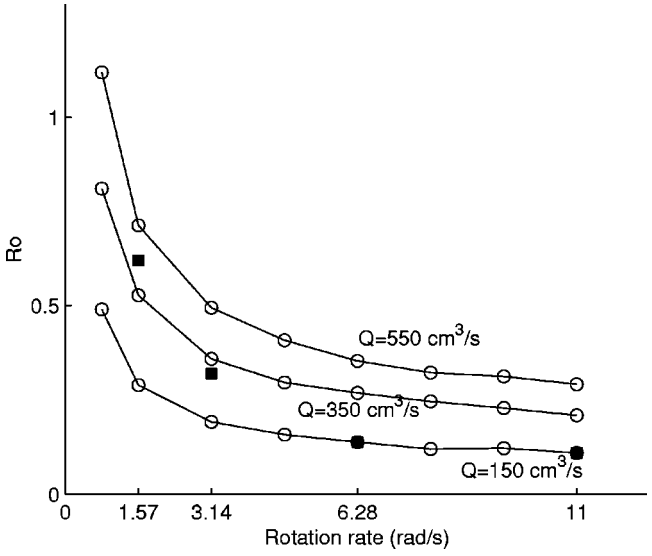

FIG. 2. Range of Rossby number as a function of rotation and pumping rates. The solid squares are points where the hot film data were obtained.

B. Flow development

When the pumping was switched on after the water had reached rigid body rotation, the subsequent development of the flow provided evidence of an inverse cascade. Small anticyclonic (counter-rotating) vortices and cyclonic (co-rotating) vortices formed above the inlet and outlet holes, respectively, and like-sign vortices merged, cascading energy to the larger scales, as Fig. 3 illustrates. Simultaneously, the radially outward flux from the pumping generated a strong counter-rotating jet between the forcing rings. The jet grew in strength until the torque from the pumping was balanced by the dissipation in the top and bottom boundaries (see Appendix B 3). This behavior was observed for all but the lowest rotation rate examined, $\Omega=0.79$ rad/s, where the merging never occurred.

The vortices that formed above the forcing holes interacted with their immediate neighbors in groups of two or three. For instance, a group of three anticyclones would start to orbit each other, and then the vortex centers would move towards the center of the trio, thus creating an elongated structure similar to a backwards ''S.'' The new vortex would intensify with lobes from the ''S'' wrapping around the central core of the vortex. The orbiting and merging steps repeated with the larger structures until the interactions with the walls became important.

C. Steady-state fields

In the asymptotic state, the vortices are advected by the anticyclonic azimuthal jet, and they interact with the walls as well as with one another (Fig. 4). The jet divides the flow into a predominantly cyclonic ($\omega>0$) region near the outer rim of the annulus, and an anticyclonic ($\omega<0$) region near the inner rim. The background shear also changes sign with radius, but at a different value of the radius, as discussed in Appendix B.

The cyclonic and anticyclonic regions of the flow are populated with large scale vortices that are advected by the jet. These vortices are visible in Figs. 4(b)–4(d), but they are absent at the lowest rotation rate [Fig. 4(a)]. These large vortices are the result of the inverse cascading described in the previous section. At the lower rotation rate in Fig. 4(b), where the flow is 3D, the cascade stops at an intermediate scale, allowing the presence of two large cyclones which do not interact with each other. Small ($\sim$1 cm) short-lived cyclonic structures occur in the anti-cyclonic region and vice versa in Figs. 4(a) and 4(b), while such vortices are absent in the more 2D flows. [In the 3D flows in Figs. 4(a) and 4(b), the images are of course 2D slices, and vortices are randomly oriented with respect to this plane.] At higher rotation rates, the cascade goes to larger scales, and the size of the largest vortex increases correspondingly; then any vortex of the same sign as the largest vortex will eventually merge with it.

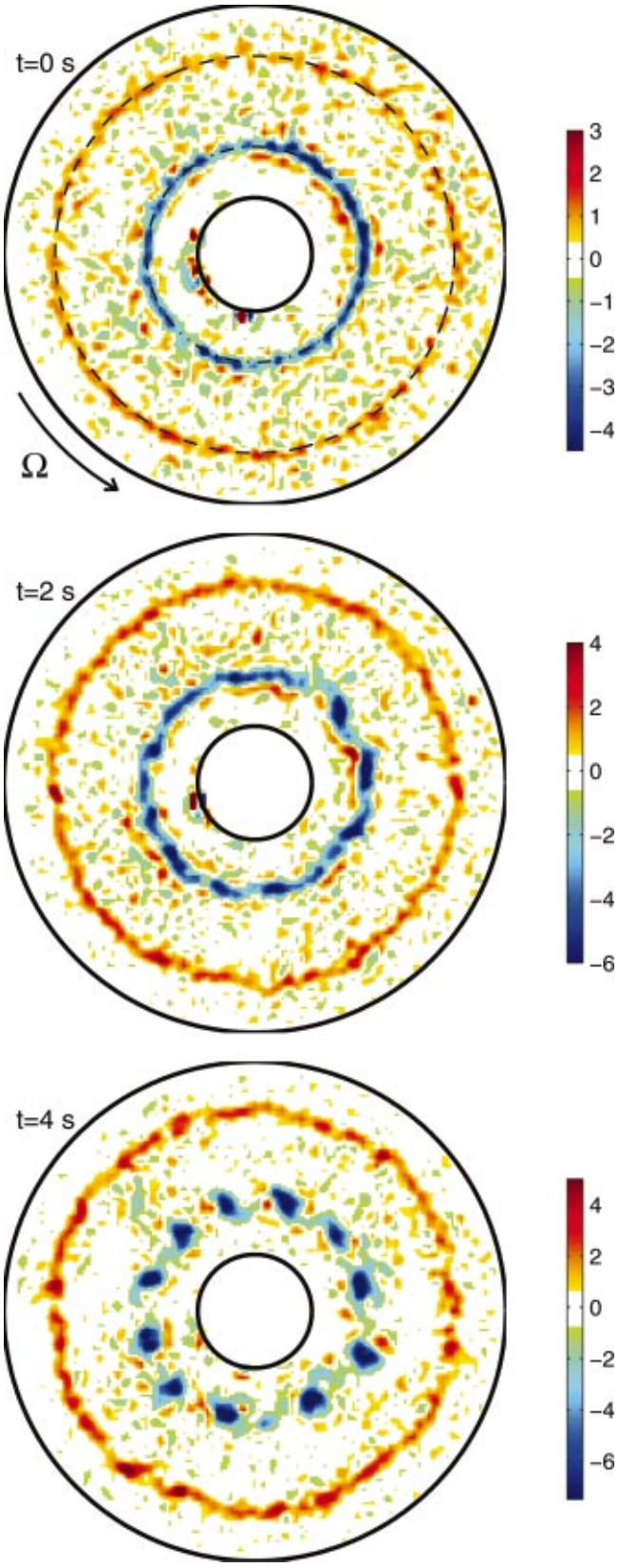

FIG. 3. (Color) Development of a quasi-2D flow at small Rossby number ($Ro=0.14$, $\Omega=1.57$ rad/s, $Q=150$ cm^3/s). A ring of anticyclones (blue) initially formed above the inlet holes, and cyclones (red) formed above the outlets. The interaction between vortices caused them to elongate and create spiral structures. The vorticity is shown only for values significantly above the noise level, and the limits on the color scale increase with time, indicating higher value of vorticity.

Similar dynamics exist on the anticyclonic side of the jet, although the anticyclones are constrained to being smaller by the geometry of the annulus.

As noted by Marcus,[24] 2D vortices in rapidly rotating flows can persist only in regions where the vorticity is of the same sign as the background shear. Near the outer wall, the circulation from the large cyclone produces a region of anticyclonic vorticity because the velocity gradient is reversed. The converse is true for the anticyclones near the inner wall. In the 2D flows, these regions of reversed vorticity grow into intense coherent structures which are in a region of adverse shear [see the compact intense vorticity patches in Figs. 4(c) and 4(d)]. Because these intense vortices are produced in regions of adverse shear, they are ejected radially across the mean jet into the region where their vorticity is of the same sign as the background shear.

Closeup sequences of ejection events are shown for the low and high rotation cases in Figs. 4(e) and 4(f). In these figures, a square section of the tank is visualized to give a higher spatial resolution of the flow. The mean clockwise (anticyclonic) jet, indicated by the curved arrow in Fig. 4(e) at $t=0$ s, is near the center of the channel, while vortices on either side of the jet are advected by it. In the low rotation (3D) case of Fig. 4(e), two ejection events can be followed: A cluster of small anticyclones (blue) orbiting each other forms at the outer (right hand side) wall, as the cyclonic (red–yellow) structure sweeps past. This cluster, marked with the circle at $t=1.0$ s, stretches radially and some of the fluid is carried inward (to the left). A similar process happens near the inner wall as the strong anticyclone (blue) causes a cyclonic (red) ejection (see the circle at $t=3.0$ s).

In the high rotation case [Fig. 4(f)], the ejecting anticyclone forms at the outer wall and grows to about 10 cm in size before being transported across the jet into the anticyclonic region of the flow. This anticyclone is connected to a thin anticyclonic region near the wall, and it grows by drawing fluid from this boundary region. In the last frame ($t=0.9$ s), it appears that this vortex is being elongated and sheared by the jet. For the conditions of this sequence, the maximum velocity in the jet can reach 80 cm/s near the center and has to go to zero at the edge. Therefore the velocity gradients can be quite large, and the shear felt by an ejecting vortex can be very high.

The sequence in Fig. 4(f) also shows several cyclones being advected by the jet. The cyclones reach the region of favorable shear faster than the anticyclones, so they are more likely to preserve their shape and to get carried azimuthally without losing their coherence (see Appendix B). Other asymmetries also exist between the cyclonic and anticyclonic ejections, although a detailed study of those will be left for future work. The size of the ejecting vortices varies with rotation and pumping rate; these vortices are always small in the 3D case, while the 2D vortices can have a range of different sizes and strengths.

The ejection events and the later merging of ejected vortices with the large coherent structures correspond to dynamics that are nonlocal in wavenumber space, that is, the interaction between structures of very different sizes. The ejection of a vortex from a wall is a process by which energy from

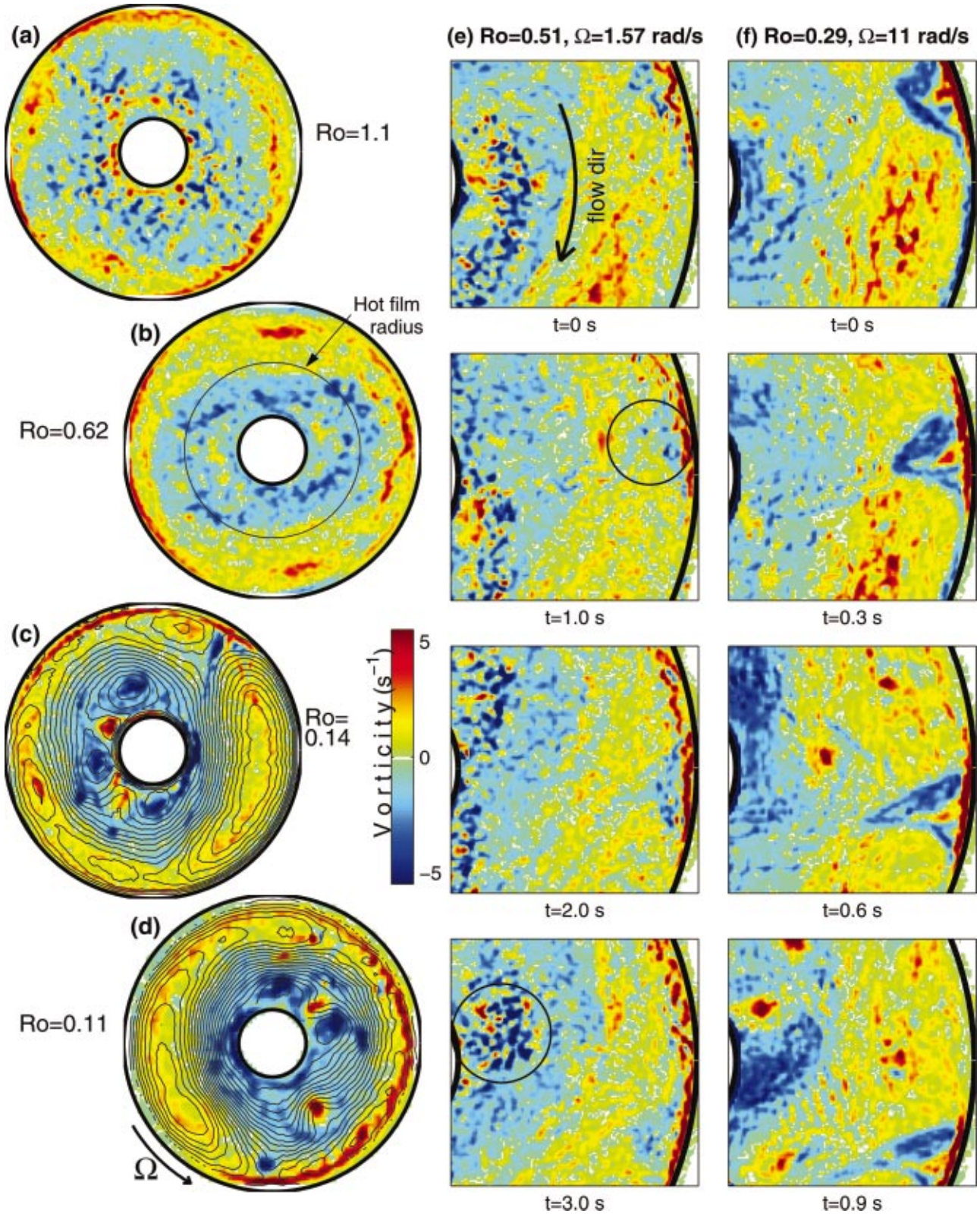

FIG. 4. (Color) Vorticity images and stream function contours for different experimental conditions: (a) $Ro=1.1$, $\Omega=0.79$ rad/s, $Q=550$ cm^3/s. (b) $Ro=0.62$, $\Omega=1.57$ rad/s, $Q=450$ cm^3/s. (c) $Ro=0.14$, $\Omega=6.28$ rad/s, $Q=150$ cm^3/s; streamline spacing is 16 cm^2/s. (d) $Ro=0.11$, $\Omega=11.0$ rad/s, $Q=150$ cm^3/s; streamline spacing is 20 cm^2/s. The color bar applies to parts (a)–(d). A mean rotation was subtracted from the streamfunctions to place the viewer in the frame of the mean flow. The two panels on the right show ejections for the 3D flow, (e) $Ro=1.51$, $\Omega=1.57$ rad/s, $Q=350$ cm^3/s, and for the 2D flow (f) $Ro=0.29$, $\Omega=11.0$ rad/s, $Q=550$ cm^3/s. See text for descriptions of the events inside the circles.

the largest scale structures is injected back at a smaller scale. Once a vortex is ejected, it can be sheared by the mean jet [e.g., the anticyclone near one o'clock in Fig. 4(c)] or it can cross the jet and merge with the large vortices on the other side, thus cascading energy back up to the large scales. The existence of strong nonlocal interactions has been found to increase the amount of intermittency in numerical simulations,[25] which is consistent with our observations.

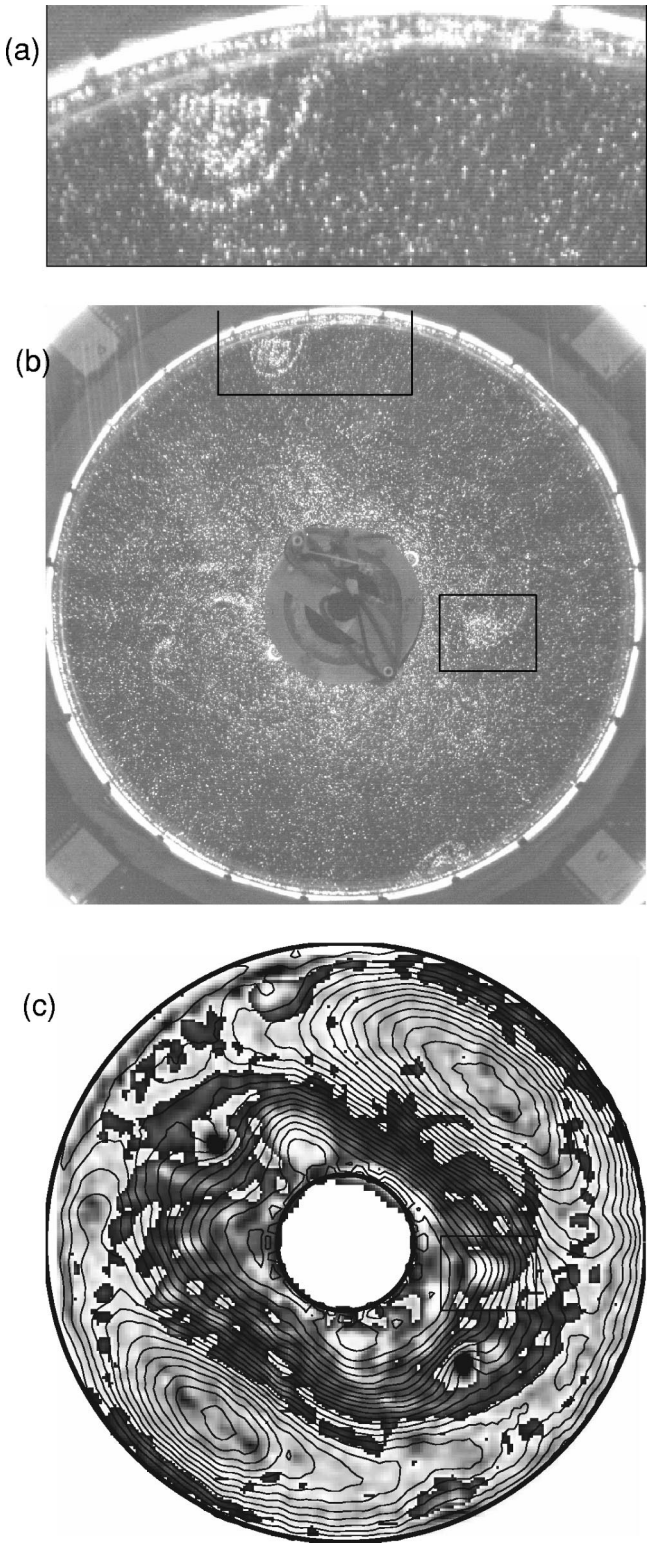

FIG. 5. (a) Close up snapshot showing particles ejected from near the outer wall into a spiral structure. (b) Snapshot of the annulus; the box at the top is the region shown close up in (a), and the box on the right is another group of particles in a vortex. (c) Stream function and vorticity fields corresponding to (b). $Ro=0.14$, $\Omega=6.28$ rad/s, and $Q=150$ cm^3/s; streamline spacing is 19 cm^2/s. In part (c), light structures surrounded with a dark area are anticyclonic, while dark structures surrounded by a light area are cyclonic.

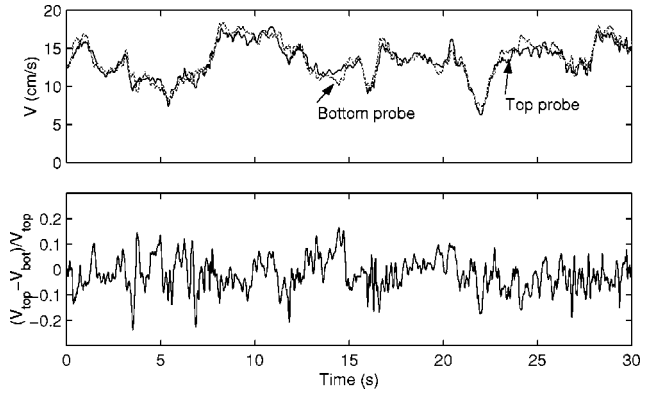

FIG. 6. Velocity at top and bottom of the annulus for a flow with $Ro=0.05$ ($Q=125$ cm^3/s, $\Omega=15.7$ rad/s, $Re=1.1\times10^4$); the two signals have a 94% correlation. The relative difference is shown in the lower graph; the rms difference between the two signals is 0.8 cm/s.

Fluid parcels are observed to advect with the vortices, as expected for 2D inviscid flow (ideal flows), as illustrated in Fig. 5. This image was taken shortly after starting the pumping, so heavier particles were still collected near the outer wall where they centrifuged in the absence of turbulent mixing at the early stages. The particle ejection can also be followed in the vorticity plots, where groups of particles can be seen to remain within a vortex as it crosses the center of the jet (see the box on the right in Fig. 5).

D. Two-dimensionalization

The two-dimensionality of the flow at high rotation rate was tested by comparing the signals from two hot film probes separated vertically by 18 cm: One probe was inserted 1 cm below the top lid, while the other was inserted 1 cm above the bottom; the two probes were at the same radial and azimuthal coordinates. In the 3D case, the time series obtained from the two probes differed greatly, while in the low Rossby number quasi-2D case, the velocity signals measured by the top and bottom probes were highly correlated, as Fig. 6 illustrates. The large scale variations are the same for the two probes, as the top graph in Fig. 6 illustrates, while the small high frequency fluctuations differ, as the lower graph in Fig. 6 illustrates.

E. Effect of vortices on time series

The validity of Taylor's frozen turbulence hypothesis is discussed in Appendix A, and the time-averaged velocity and vorticity results are presented in Appendix B. In this subsection, we consider the relation between the fluctuations in the time series and the structures in the flow. A snapshot of the vorticity field is shown mapped onto a rectangle in Fig. 7(a). A compact cyclonic vortex with a dark center is near $\pi/2$; this vortex leads to the sharp drop in the azimuthal velocity that can be seen in Fig. 7(b). Similarly, the anticyclone ejected from the outer wall near $5\pi/4$ leads to a drop in the azimuthal velocity.

The velocity time series measurements all display large dips, as illustrated in Figs. 6(a) and 7(b). Superposed on those variations are high frequency ''turbulent'' fluctuations

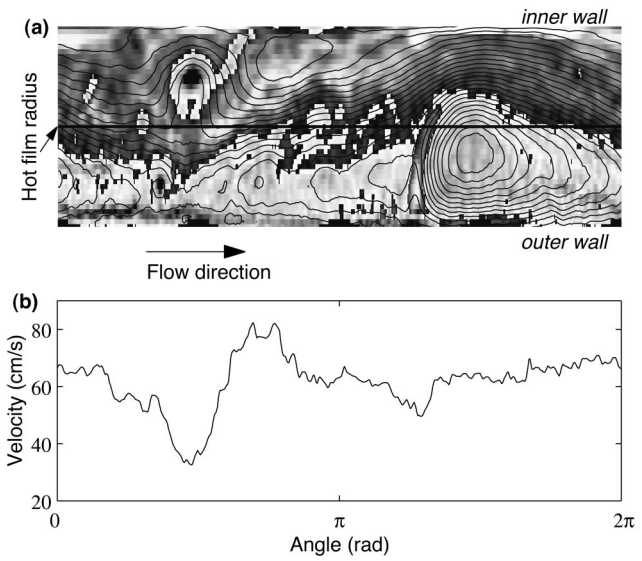

FIG. 7. (a) Snapshot of the vorticity field mapped onto a rectangle; vortices with a dark center correspond to cyclones, while vortices with a light center are anticyclones. (b) Azimuthal velocity at the hot film radius. $Ro=0.29$, $\Omega=11.0$ rad/s, $Q=550$ cm^3/s; streamline spacing in (a) is 56 cm^2/s. Gray scale in (a) same as in Fig. 5(c).

corresponding to the smaller structures being swept past the probe. It is difficult to distinguish between the 2D and the 3D flows directly from the time series, but the distinction is pronounced in the high order statistics (Sec. IV C).

IV. STRUCTURE FUNCTIONS

A. Length scales

The scaling arguments for the structure functions should apply in the inertial range. For 2D turbulence, this range is divided into a forward enstrophy cascade for wavelengths λ smaller than the injection length λ_i, and an inverse energy cascade for $\lambda>\lambda_i$.[26] Our injection scale is 1 to 2 cm (the distance between the inlet holes is 1 cm, the distance between the outlet holes is 2 cm). Therefore, we expect both a forward cascade limited by the Kolmogorov length λ_k at the small scales, and an inverse cascade up to the Rhines length λ_β.

The Kolmogorov dissipation scale λ_k is given by the fluid viscosity and the mean energy transfer rate ε

$$\lambda_k=\left(\frac{\nu^3}{\varepsilon}\right)^{1/4}. \tag{3}$$

Assuming small-scale isotropy, we estimate ε by

$$\varepsilon=15\nu\left\langle\left(\frac{\partial u}{\partial x}\right)^2\right\rangle=15\nu\int k^2E(k)dk. \tag{4}$$

The value of λ_k remains nearly constant at $\lambda_k\simeq0.07$ cm for all rotation and pumping rates in the hot-film measurements. The digital sampling rate of the hot-film probes, $f=150$ Hz, corresponds to a spatial scale of $U/f\simeq0.1$ cm, which is close to the value of λ_k; however, our spatial resolution is limited by the length of the probe's sensing element, 0.3 cm.

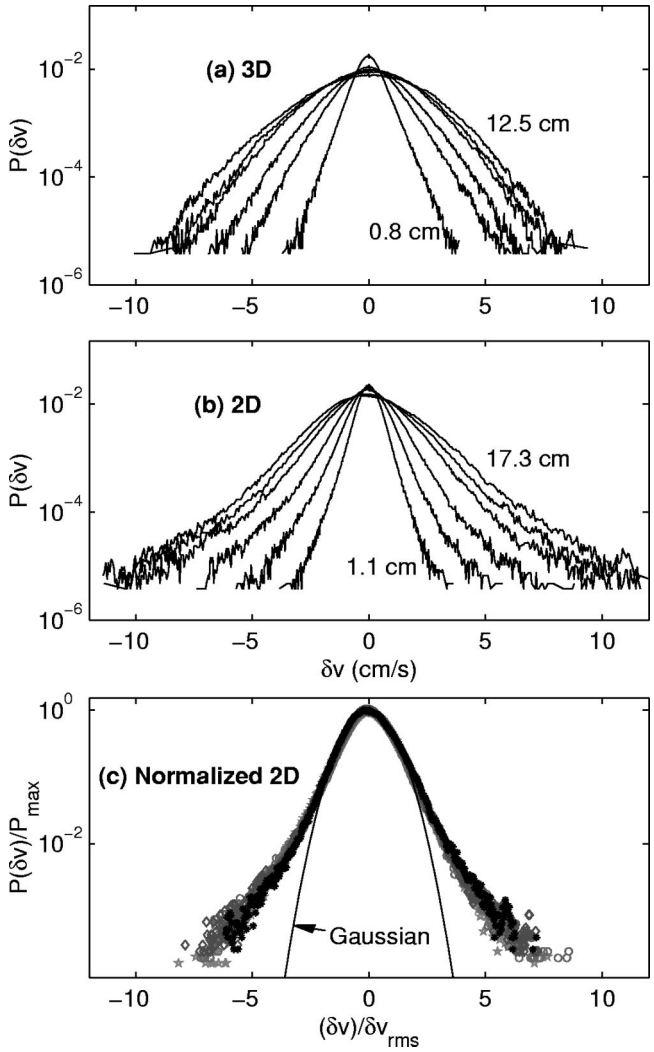

FIG. 8. Velocity difference PDFs for: (a) $Ro=0.62$ (1.57 rad/s, 450 cm^3/s) for $d=0.8$, 2.4, 3.9, 7.0, 8.5, and 12.5 cm; (b) $Ro=0.11$ (11.0 rad/s, 150 cm^3/s) for $d=1.1$, 2.3, 4.6, 9.2, 12.7, and 17.3 cm. The PDFs for small and large separations are clearly different for the 3D flow, while the PDF for the 2D flow has the same shape for different separations, as (c) illustrates by rescaling the width by the rms velocity and the probability P by the maximum probability (Refs. 5 and 29).

The Rhines length λ_β can also be estimated from the time series by using Eq. (2). For our data, λ_β is 18 cm for the 2D flow (state I) and 40 cm for the more 3D flows (state IV).

B. Probability distribution functions

The PDFs of the velocity differences $\delta v(d)$ for several separations (d) at low and high rotation rates are shown in Fig. 8. The PDFs for low rotation rates shift from exponentials (in the tails) at small separations to Gaussians at large separations, as expected for 3D turbulence. In contrast, the PDFs for 2D turbulent flow preserve their shape over a wide range of separations, indicating a self-similar flow. Further, the PDFs for 2D turbulence are non-Gaussian, which is consistent with numerical simulations by She *et al.*[27] and by Farge *et al.*,[28] who found that coherent structures cause the deviation from Gaussianity.[29]

The self-similarity of the 2D turbulent flow might be due

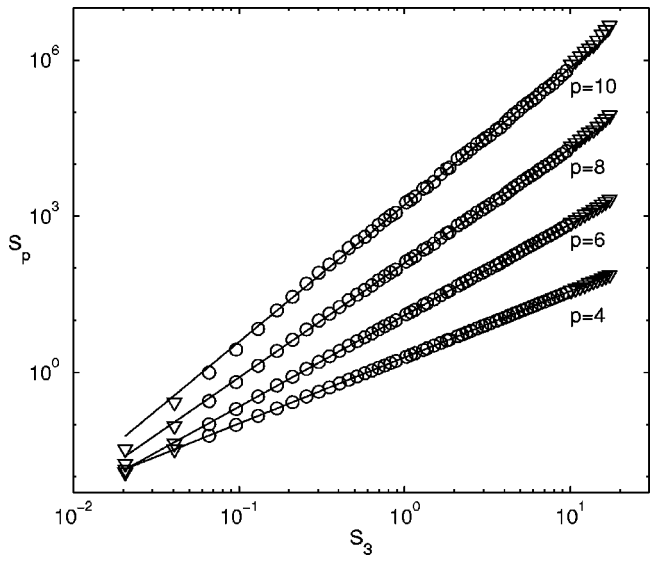

FIG. 9. Extended self-similarity (ESS) plots for a 3D turbulent flow (Case IV in Table I): The exponents ζ_p/ζ_3 (with $\zeta_3=1$ for 3D turbulence) are given by the slope of the lines. The smallest scale is approximately 0.5 cm, and the largest scale is about 15 cm.

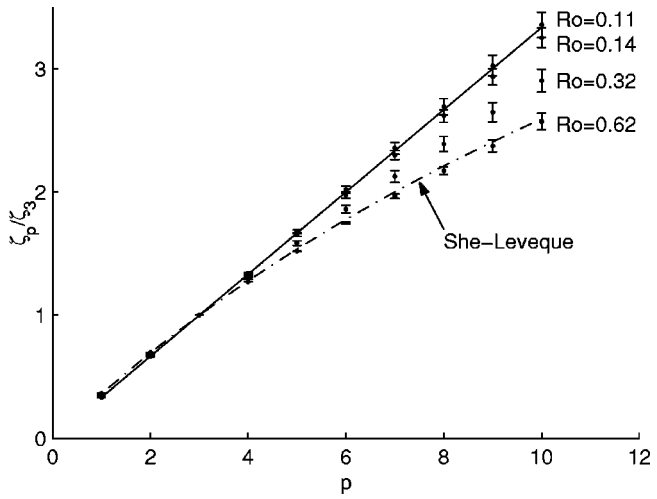

FIG. 10. Structure function exponent ratio as a function of order p for flows ranging from 2D ($Ro=0.11$, Case I in Table I) to 3D ($Ro=0.62$, Case IV).

to the existence of coherent vortices at all the scales in the inertial range (see Sec. III C), or alternatively to an inverse cascade which preserves the coherence of vortices as they merge and grow. For the 3D flow, the coherent vortices appear to exist only at small scales, which may be why the PDFs exhibit a strong scale dependence.

C. Structure function scaling

The scaling exponents ζ_p are obtained by the method of extended self similarity (ESS):[16] Slopes of log–log plots of S_p vs S_3 yield values for ζ_p/ζ_3, as Fig. 9 illustrates. (The determination of the exponents for the 2D flow was reported in an earlier paper, where we used $S_3=\langle|\delta v|^p\rangle$ since S_3 changes sign,[5] as shown in Appendix B 1.) The fits are good for both the 2D and 3D cases for length scales in the range $0.5<\lambda<15$ cm. This scaling region is bounded by λ_k and λ_β but never quite reaches either. However, the curvature of our annulus distorts structures larger than about 15 cm, so it is not surprising that we see deviations from the linear fit at those scales.

The dependence of the exponent ratio ζ_p/ζ_3 on order p for $p\leqslant 10$ is shown in Fig. 10 for four Rossby numbers. The scaling for the most 2D flow is linear in p, as expected for a self-similar flow, as shown in Ref. 5, while for higher Rossby number, an increasing departure from self-similar behavior develops. Care must be taken in interpreting Fig. 10 because ζ_3 decreases from 3/2 for low Rossby number flow (e.g., $Ro=0.11$), as shown in Ref. 5, to unity for 3D turbulence (e.g., $Ro=0.62$).[6] The most 3D flow falls on the She–Lévêque curve, matching data from simulations and other experiments on 3D turbulence.[30,31] This suggests that structure function exponents are a reliable measure of the extent to which a flow is 2D or 3D. The values of ζ_p/ζ_3 for the different conditions of our flow are given in Table II, along with values for Couette–Taylor flow,[18] another flow with strong rotation, but one in which the Rossby number is not small. For comparison we also include scaling exponents for the atmospheric boundary layer.[32]

V. HIERARCHICAL SYMMETRY

We have seen that the structure function exponents shift from a linear scaling with order p at high rotation rate to the typical 3D behavior for the low rotation rate, falling increasingly lower than $p/3$ with increasing p. This departure from self-similarity for the 3D case has been studied extensively in previous work. To learn more about the internal structure of the flow, we consider the She–Lévêque[17] model of turbulence. This model assumes an internal organization of the flow, which consists of a hierarchy of structures ranging from strong highly intermittent ones (such as collapsed vortices) to weaker more common events.

The hierarchical structural model proposes two tests, the β-test and the γ-test, which allow us to understand better the relationship between the structures of different intensities in our flow. The tests concern the scaling of the hierarchy of functions $F_p(d)=S_{p+1}(d)/S_p(d)$. The function F_p is the mathematical expectation value for a family of weighted probability distribution functions, $Q_p(\delta v_d)=|\delta v_d|^p P(\delta v_d)/\langle|\delta v_d|^p\rangle$, or the mean fluctuation amplitude with respect to this family of distributions. For higher p, $Q_p(\delta v_d)$ is peaked at higher intensity of the fluctuations δv_d. Therefore, these functions describe the intensity of fluctuations in the flow, with higher order F_p describing the more intermittent, larger, fluctuations. The model proposes the scaling

$$F_{p+1}(d)=A_p F_p(d)^\beta F_\infty(d)^{1-\beta}, \tag{5}$$

where $0\leqslant\beta\leqslant 1$ is a constant, A_p is independent of d, and where

$$F_\infty(d)=\lim_{p\to\infty}\langle|\delta v_d|^{p+1}\rangle/\langle|\delta v_d|^p\rangle \tag{6}$$

characterizes the most intermittent structures.

TABLE II. Values of ζ_p/ζ_3 for different Rossby numbers, compared with values from other experiments.

		Current experiments (cf. Table I)				Couette–Taylor[a] (Ref. 18)	Atmospheric flow (Ref. 32)	She–Lévêque (Ref. 17)
p	$p/3$	$Ro=0.11$	$Ro=0.14$	$Ro=0.32$	$Ro=0.62$	$Re_\lambda \simeq 220$	$Re_\lambda \simeq 10{,}000$	
4	1.33	1.34	1.33	1.30	1.27	1.27	1.26	1.28
6	2.00	2.02	2.00	1.86	1.75	1.71	1.71	1.78
8	2.67	2.69	2.62	2.40	2.17	2.08	2.05	2.21
10	3.33	3.36	3.25	2.90	2.57	2.40	2.38	2.59

[a]Higher order ζ_p for Couette–Taylor are $\zeta_{12}=2.70$, $\zeta_{14}=3.00$, $\zeta_{16}=3.31$, and $\zeta_{18}=3.62$.

A. The β-test

In theory one needs to wait an infinite time to measure F_∞, but the difficulty is avoided by considering the ratio

$$\frac{F_{p+1}(d)}{F_2(d)} = \frac{A_p}{A_1}\left(\frac{F_p(d)}{F_1(d)}\right)^{\beta}, \tag{7}$$

which can be calculated for all values of p. The β-test consists of checking for this power law scaling. If it exists, then the hierarchical symmetry is satisfied and the value of the slope (β) in log–log plots characterizes the amount of intermittency in the flow. The β-test is applied in Fig. 11 to our 2D and 3D turbulent flows.

The value of β remained unchanged with increasing Rossby number for the cases in Table I: $\beta_{\mathrm{I}}=0.74\pm0.02$, $\beta_{\mathrm{II}}=0.78\pm0.02$, $\beta_{\mathrm{III}}=0.72\pm0.02$, and $\beta_{\mathrm{IV}}=0.76\pm0.02$. These values are lower than those reported for Couette–Taylor turbulence[18] (0.83) and turbulent free jets[19] (0.87). Our lower β are consistent with the observation that coherent structures dominate the turbulent background for all of the cases we have examined (see Fig. 4).[18,19]

The points in Fig. 11 for the 2D case fall in compact groups for each p, as expected for a self-similar flow; if the flow were perfectly self-similar, these compact groups would each collapse to a point since there is no dependence on d. In contrast, the 3D points fall on a straight line as either d or p is varied. From the results of Fig. 11 and the scaling of the structure function exponents, we conclude that the 2D flow is no less intermittent than the 3D flow, but that rotation two-dimensionalizes the intermittent structures; these structures become self-similar in the 2D case, producing a flow where vortices of all (inertial range) sizes and strengths are present.

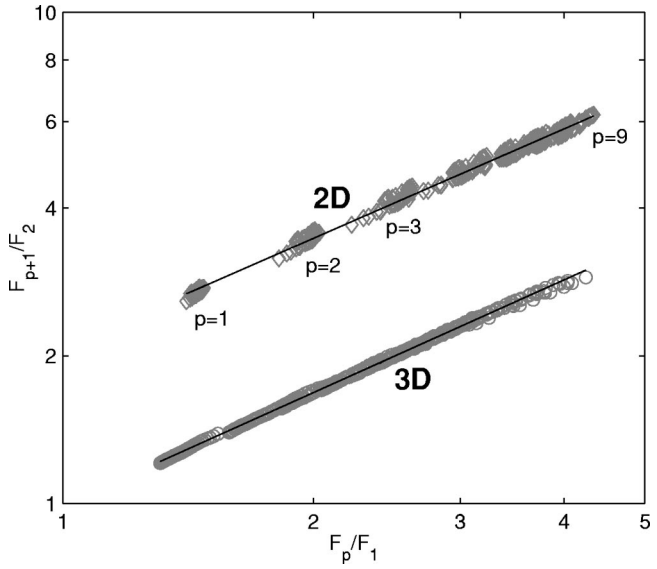

FIG. 11. β-tests for 3D and 2D turbulent flows, where a straight line indicates that the data satisfy the β-test. The curve for the 2D flow is shifted up for clarity. The slopes of these curves are $\beta=0.74$ ($Ro=0.11$) and $\beta=0.76$ (Ro=0.62).

B. The γ-test

The hierarchical structure model further assumes the scaling

$$F_\infty \sim S_3^{\gamma}(d), \tag{8}$$

where γ describes the scaling of the most intermittent structures relative to the more typical events (of the order of $S_3^{1/3}$). The meaning of γ can be understood by examining PDFs in Fig. 8 for fluctuations at different scales. The value of γ describes how fast the magnitude of the tail (characterized by F_∞) changes in response to the width of the PDFs (characterized by $S_3^{1/3}$). When $\gamma=1/3$, the tail expands in the same way as the width of the PDFs, so that the whole family of PDFs preserve their shape. This is a situation where the fluctuations of all intensities are statistically alike; the flow is globally self-similar. Another limit is $\gamma=0$, in which the magnitude of the most intermittent structures is not related to the typical fluctuation magnitude. This is the situation where the coherent intermittent structures are physically decoupled from the disordered fluctuations. An example is the randomly driven Burgers equation, where shocks are the most intermittent structures and the only dissipative structures in the limit of vanishing viscosity.

In summary, decreasing γ indicates an increasing distinction of the most intermittent structures with respect to the background flow structures. With the assumption of Eq. (8), the relative scaling exponent of the velocity structure functions ζ_p is given by[17]

$$\zeta_p = \gamma p + C(1-\beta^p), \tag{9}$$

where $C=(1-3\gamma)/(1-\beta^3)$. Given the values of β, the validity of the assumption (8) can be tested by checking that

$$\zeta_p - \chi(p;\beta) = \gamma[p-3\chi(p;\beta)], \tag{10}$$

where $\chi(p;\beta)=(1-\beta^p)/(1-\beta^3)$. From Eq. (9), it is evident that a self-similar turbulent flow can be reached in two ways: either $\beta\to1$ or $\gamma\to1/3$. According to the Hierarchical Structure model, β measures how fast the coherence of flow

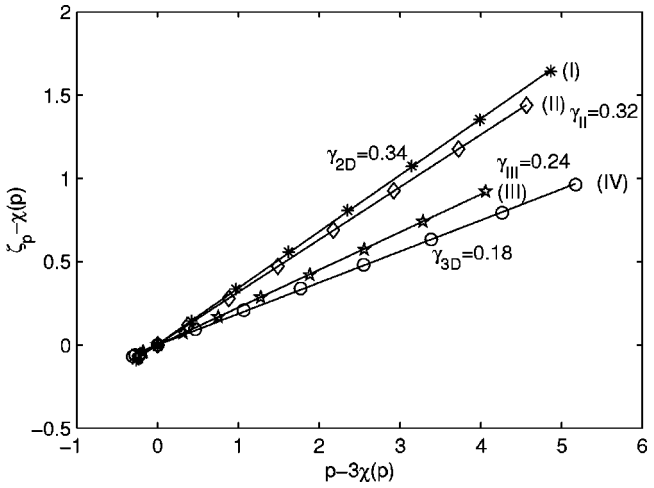

FIG. 12. γ-test for the hot film data in Table I ranging from 2D turbulence (case I, $Ro=0.11$) to 3D turbulence (case IV $Ro=0.62$). The lines are least-squares fits to the data.

structures is established for fluctuations standing out of the random background field, or how fast the coherence of the most intermittent structures is degraded with decreasing magnitude. When β approaches one, flow structures of all intensities appear alike; this similarity of all intensities implies in general the lack of coherence, or the lack of intermittency. In this scenario, γ can in principle have any value. Such a scenario has not yet been observed.

On the other hand, the relative scaling with γ approaching 1/3 is a different scenario that yields a self-similar flow. Since F_∞ is the magnitude of the most intermittent structures, γ measures how fast its magnitude (e.g., the tail of the PDFs) changes with the typical fluctuation magnitude represented by S_3 (e.g., the width in the bell-like curves in Fig. 8). This seems to be the scenario observed here: Throughout the transition from 3D to 2D turbulence, β remained unchanged ($\beta \simeq 0.75$), while γ showed a gradual increase from $\gamma_{3D}=0.18$ to $\gamma_{2D}=0.34$ (Fig. 12).

The fits for γ are robust and are independent of β within the experimental uncertainty. The value of γ_{3D} (0.18) is higher than the value reported for Couette–Taylor experiments and free jets (0.10). This is probably due to the effect of rotation, since even in our most 3D flow the rotation begins to inhibit the stretching of structures ($Ro<1$). On the other hand, the value of γ_{2D} (0.34) gives further indication of a self-similar flow. Thus the γ test helps discover a smooth transition in the degree of the synchronization between the high and low intensity fluctuations when the rotation rate increases.

VI. DISCUSSION

We have examined turbulence in a flow with constant Reynolds number ($Re_\lambda \simeq 360$) and decreasing Rossby number Ro (increasing rotation rate). At $Ro \simeq 1$, the values of the structure function exponents ζ_p were the same as found in experiments on 3D turbulence in nonrotating flows, and were in accord with the prediction of the She–Lévêque model. With decreasing Ro, the flow became more 2D and self-similar, as indicated by the velocity increment PDFs and the values of ζ_p, which attained the values $p/2$ at the lowest Ro.[5]

Application of the β and γ tests of the Hierarchical Structure model provided insight into the flow structures. The value of β (0.75) did not change with Rossby number, indicating a highly intermittent flow with a constant level of coherence, which is consistent with our visual observations of coherent vortices at all rotation rates. The vortices existed over a wider range of length scales as the flow became 2D, probably because 2D vortices could not stretch and collapse into filaments. The γ-test supported this observation: At $Ro \simeq 1$, we obtained $\gamma=0.18$, while at $Ro=0.11$, we found $\gamma \simeq 1/3$, as required for self-similar turbulence.

We observe that for all rotation rates examined, there are coherent vortices with sizes ranging upward from the injection scale. At high rotation rates, the large intense vortices become more stable and the 2D flow becomes self-similar yet remains intermittent even though vortices cannot stretch. Vortices of all scales exist within the inertial range, and this leads to statistics of the velocity increments that are far from Gaussian even at large separations.

There are many questions that warrant further study. The role of the beta plane (sloped bottom) should be examined by varying both the sign and magnitude of the slope of the bottom of the annulus. The injection length scale and the configuration of the forcing should each be varied, and the effect of dissipation should be examined by changing the depth of the fluid in the annulus. Also, the role of the sidewalls should be investigated by changing the diameter of the annular tank.

ACKNOWLEDGMENTS

The authors acknowledge helpful discussions with P. S. Marcus. The work at the University of Texas was supported by Grant No. N00014-98-1-0047 from the Office of Naval Research. Z.-S.S. acknowledges partial support from the Minister of Education in China and Project No. 10032020 supported by the NSFC.

APPENDIX A: TIME SERIES ANALYSIS

It is common to use Taylor's frozen turbulence hypothesis to convert a time series into a spatial record using the mean flow velocity. This is applicable for flows with a turbulent intensity $Tu=\sqrt{\langle u^2\rangle}/\langle u\rangle \leqslant 10\%$. In quasi-2D flows, this limit might be higher.[33] In our experiments, *Tu* reached 17% at the lowest rotation rate of our hot film velocity measurements, 1.57 rad/s; we did not make hot film measurements at lower rotation rates because the mean velocity becomes very low, making *Tu* much larger. At the highest rotation rates, it was lower than 10%. To gauge the effect of the high turbulent intensity, a technique similar to that of Pinton and Labbé[34] was applied to reconstruct the spatial information: We first cumulatively summed over the velocities, then found the corresponding position for each time step, and finally interpolated onto an equally spaced grid. This method effectively uses the instantaneous rather than the mean velocity to make the transformation from temporal

to spatial information. Applying this technique did not affect our conclusions, probably because of the large separation of scales between the large fluctuations and the scale of the structures of interest (see Sec. III). The results presented here were obtained using Taylor's hypothesis in the usual way.

The structure functions were calculated using the method of She *et al.*:[18] A histogram of the velocity differences for a given separation was first generated to approximate the probability distribution function (PDF). In order to reduce the sensitivity to random noise, the PDF was smoothed using a weighted local average. Then $S_p(d)$ was obtained by raising the smoothed PDF to the power p and calculating the mean value. This method for obtaining S_p is fast to implement and is less sensitive to erroneous measurements than using the raw data for velocity differences.

Structure function exponents were determined by the extended self similarity (ESS)[16] technique: Values of ζ_p/ζ_3 were obtained from slopes of log–log plots of $S_p(d)$ vs $S_3(d)$. For a self-similar flow, the exponent ratio should increase linearly with p,[6] as we find for our 2D flow, while deviations from linearity indicate scale-dependent statistics, as we find for our 3D flow. In an earlier direct analysis of 2D turbulence,[5] we obtained $\zeta_p = p/2$ from log–log plots of S_p vs d, but we do not report here the results of a direct analysis of the data for 3D turbulence because of the absence of a scaling range.

The points plotted in Fig. 10 are the average values for the two probes over all realizations at the same conditions. The error bars correspond to the standard deviation from the different experimental runs. In order to test the convergence of our fits, the data were divided into sets of shorter time series and the structure function routines were run on those subsets. For time series longer than $N = 2.5\times 10^5$ points, the spread in the calculated exponents (ζ_{10} in particular) with record length for a particular time series was comparable to the spread from separate runs, the latter being due to systematic errors during a given run. It was, therefore, more advantageous to take several independent realizations of the same flow rather than longer time records.

APPENDIX B: MEAN FLOW QUANTITIES

1. Skewness

We computed the skewness of the velocity differences

$$\xi = \frac{S_3}{S_2^{3/2}}, \tag{B1}$$

using the hot film probe data (Fig. 13). Given that the structure functions S_2 and S_3 display a power law scaling with d as $S_p \sim d^{p/2}$, the skewness ξ should display a region independent of the separation d. The data do not show a region of constant skewness, but ξ is small in the range in which the structure function exponents were determined. Further, note that the ESS analysis was done using the absolute value of δv, thus reducing the variations in ξ. In the homogeneous isotropic case, the sign of S_3 should reflect the direction of the energy cascade.[5]

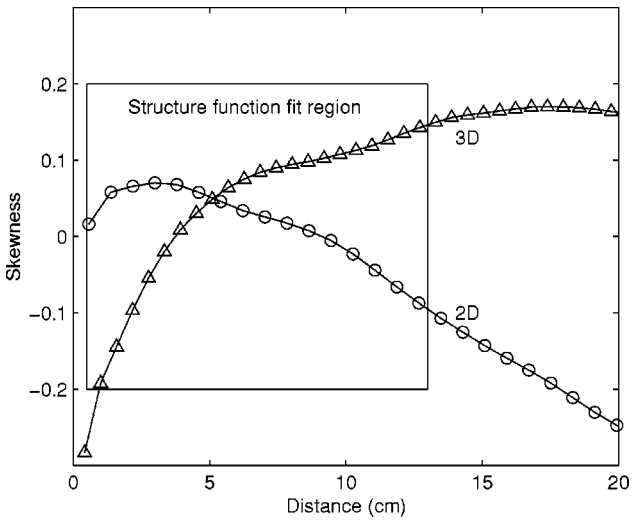

FIG. 13. Skewness of the velocity differences in the 2D and 3D cases. The box shows the approximate fitting region of the structure functions.

Finally, at large separations, we expect that the shape of the tank, possible side wall effects, and departures from isotropy affect the scalings, and we are unable to draw quantitative conclusions about the significance of the skewness.

2. Radial profiles

We have used the visualization data to determine the radial dependence of the azimuthally averaged velocity, vorticity, and shear, as presented for two cases in Fig. 14. The shear in a polar coordinate system is defined as

$$\sigma_{r\phi} = \frac{r}{2}\left[\frac{\partial(v_\phi/r)}{\partial r} + \frac{1}{r}\frac{\partial v_r}{\partial \phi}\right], \tag{B2}$$

where v_ϕ is the azimuthal velocity and v_r is the radial velocity. Averaging spatially over many images, the second term in Eq. (B2) was found to be negligible compared to the first term, even though the second term was typically dominant in a given snapshot; hence the graphs show only the first term

$$\overline{\sigma}_{r\phi} = \frac{r}{2}\frac{\partial(v_\phi/r)}{\partial r}. \tag{B3}$$

For both the 2D and 3D cases, the jet fills the width of the annulus, and the location of the velocity maximum moves slightly towards the outside of the annulus as the pumping increases; thus for a fixed value of the maximum velocity, the total kinetic energy in the flow increases since a larger volume of water is displaced at larger radii.

The 2D vorticity profile displays a central region where the vorticity of the flow increases almost linearly. This region corresponds to the region with the strong jet, away from the large coherent vortices that travel near the inside and outside walls. The signature of the vortices is found to be a plateau of vorticity near the walls. For the 3D flow, the central region is not linearly increasing, but one can still differentiate between the central region with a strong jet and regions to either side with vortices.

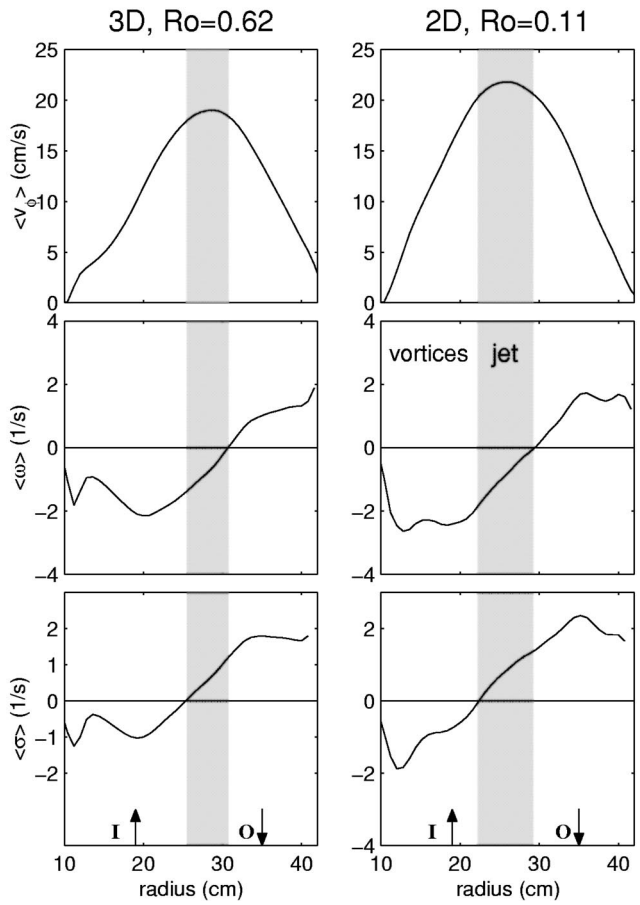

FIG. 14. Radial dependence of azimuthally averaged quantities: azimuthal velocity (v_ϕ), vorticity (ω), and mean shear ($\sigma_{r\phi}$), for the 2D ($\Omega=11.0$ rad/s, $Q=150$ cm^3/s) and 3D ($\Omega=1.57$ rad/s and $Q=550$ cm^3/s) cases. The shaded areas correspond to regions where the vorticity is negative and the shear is positive, where coherent long-lived vortices cannot survive. See text for discussion.

The shape of the curves for the mean shear is similar to the shape of the vorticity curves, but the shear ($\overline{\sigma}_{r\phi}$) changes sign at a radial location different from that for the vorticity (ω). The large coherent vortices of Fig. 4 are only stable in the region where $\overline{\sigma}_{r\phi}$ and ω are of the same sign, as discussed by Marcus.[24] In the region where the shear is adverse, the vortices can dissipate by shedding filaments of fluid, or by elongating in the plane of the flow and losing their coherence.

Finally, note that the velocity, vorticity, and shear profiles might depend on the location of the rings of forcing holes; this possible dependence will be examined in a future study.

3. RMS velocity

The mean velocity of our flow is set by a balance of the torque due to the Coriolis force and the torque from the Ekman dissipation. Sommeria *et al.*[20] derived an approximate formula for the maximum velocity based on this balance

$$v_\phi = \left(\frac{b}{a^2}\right)^{1/3} K(Q\Omega)^{2/3}, \tag{B4}$$

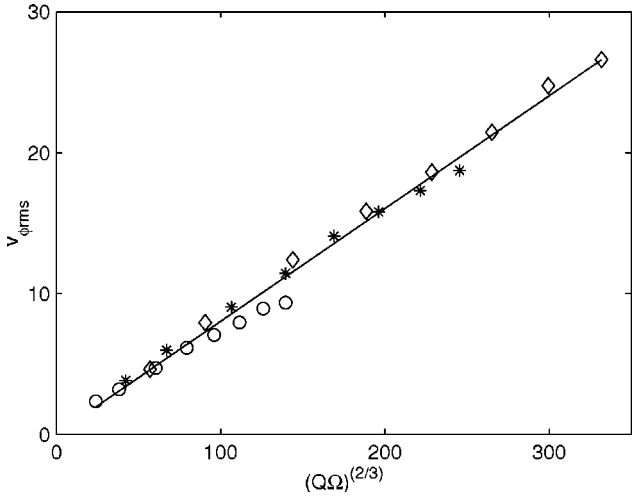

FIG. 15. RMS azimuthal velocity plotted vs $(Q\Omega)^{2/3}$ for $Q=150$, 350, 550 cm^3/s (○, ∗, and ◇, respectively), and $0.78\leqslant\Omega\leqslant11.0$ rad/s. The solid line is a linear fit to the data, giving a slope of 0.083, and an intercept of 0. The corresponding $b/a^2=0.37$.

where a and b are dimensionless constants that depend on the shape of the jet, and K is a constant that depends on the geometry of the annulus and fluid viscosity: $K=(sd^2/2\pi^2\nu h_0\langle r\rangle^2)^{1/3}$, where s is the slope, d is the distance between the forcing holes, h_0 is the mean height, and $\langle r\rangle$ is the mean radius. For each set of control parameters, we determined root-mean-squared (rms) velocity from PIV data, and the result is shown in Fig. 15. The shape of the jet varied significantly over the wide range of pumping and rotation rates, so the parameters a and b were not constant. Nevertheless, the observed linear dependence of $(v_\phi)_{\rm rms}$ on $(Q\Omega)^{2/3}$ supports the idea that the Ekman dissipation is the main mechanism limiting the azimuthal velocity.

[1] J. Paret and P. Tabeling, "Intermittency in the two-dimensional inverse cascade of energy: Experimental observations," Phys. Fluids **10**, 3126 (1998).
[2] W. B. Daniel and M. Rutgers, "A measurement of intermittency in the enstrophy and energy cascades of forced 2D turbulence," Bull. Am. Phys. Soc. **44**, 16 (1999); W. B. Daniel, "Experiments with flowing soap films: Intermittency, structure, and rheology in two-dimensional turbulence," Ph.D. dissertation, Ohio State University, 2001.
[3] M. Lesieur, *Turbulence in Fluids*, 3rd ed. in *Fluid Mechanics and its Applications* (Kluwer Academic, Dordrecht, 1997).
[4] J. Pedlosky, *Geophysical Fluid Dynamics* (Springer Verlag, New York, 1979).
[5] C. N. Baroud, B. B. Plapp, Z.-S. She, and H. L. Swinney, "Anomalous self similarity in a turbulent rapidly rotating fluid," Phys. Rev. Lett. **88**, 114501 (2002).
[6] U. Frisch, *Turbulence, The Legacy of A. N. Kolmogorov* (Cambridge University Press, Cambridge, 1995).
[7] N. K.-R. Kevlahan and M. Farge, "Vorticity filaments in two-dimensional turbulence: Creation, stability and effect," J. Fluid Mech. **346**, 49 (1997).
[8] G. S. Lewis and H. L. Swinney, "Velocity structure functions, scaling, and transitions in high-Reynolds-number Couette–Taylor flow," Phys. Rev. E **59**, 5457 (1999).
[9] G. Boffetta, A. Celani, and M. Vergassola, "Inverse energy cascade in two-dimensional turbulence: Deviations from Gaussian behavior," Phys. Rev. E **61**, R29 (2000).
[10] E. D. Siggia and H. Aref, "Point-vortex simulation of the inverse energy cascade in two-dimensional turbulence," Phys. Fluids **24**, 171 (1981).
[11] L. M. Smith and V. Yakhot, "Bose condensation and small-scale structure

generation in a random force driven 2D turbulence,'' Phys. Rev. Lett. **71**, 352 (1993).
[12]P. Vorobieff, M. Rivera, and R. E. Ecke, ''Soap film flows: Statistics of two-dimensional turbulence,'' Phys. Fluids **11**, 2167 (1999).
[13]T. S. Lundgren, ''A small-scale turbulence model,'' Phys. Fluids A **5**, 1472 (1993).
[14]Y. Zhou, ''A phenomenological treatment of rotating turbulence,'' Phys. Fluids **7**, 2092 (1995).
[15]V. M. Canuto and M. S. Dubovikoy, ''Physical regimes and dimensional structure of rotating turbulence,'' Phys. Rev. Lett. **78**, 666 (1997).
[16]R. Benzi, S. Ciliberto, R. Tripiccione, C. Baudet, F. Massaioli, and S. Succi, ''Extended self-similarity in turbulent flows,'' Phys. Rev. E **48**, R29 (1993).
[17]Z.-S. She and E. Lévêque, ''Universal scaling laws in fully developed turbulence,'' Phys. Rev. Lett. **72**, 336 (1994).
[18]Z.-S. She, K. Ren, G. S. Lewis, and H. L. Swinney, ''Scalings and structures in turbulent Couette–Taylor flows,'' Phys. Rev. E **64**, 016308 (2001).
[19]Z.-S. She and L. Liu, ''Measuring intermittency parameters of energy cascade in turbulence,'' Acta. Mech. (to be published).
[20]J. Sommeria, S. D. Meyers, and H. L. Swinney, ''Experiments on vortices and Rossby waves in eastward and westward jets,'' in *Nonlinear Topics in Ocean Physics*, edited by A. Osborne (North-Holland, Amsterdam, 1988), pp. 227–269.
[21]T. G. Shepherd, ''Rossby waves and two-dimensional turbulence in a large-scale zonal jet,'' J. Fluid Mech. **183**, 467 (1987).
[22]The exact values of the Rossby and Reynolds numbers can vary depending on the length and velocity scales used, or on the exact definition of *Ro*, e.g., Ref. 5.
[23]C. Camdon, N. N. Mansour, and F. S. Godeferd, ''Energy transfer in rotating turbulence,'' J. Fluid Mech. **337**, 303 (1997).
[24]P. S. Marcus, ''Vortex dynamics in a shearing zonal flow,'' J. Fluid Mech. **215**, 393 (1990).
[25]J.-P. Laval, B. Dubrulle, and S. Nazarenko, ''Nonlocality and intermittency in three-dimensional turbulence,'' Phys. Fluids **13**, 1995 (2001).
[26]R. H. Kraichnan, ''Inertial ranges in two-dimensional turbulence,'' Phys. Fluids **10**, 1417 (1967).
[27]Z.-S. She, E. Jackson, and S. A. Orszag, ''Structure and dynamics of homogeneous turbulence: models and simulations,'' Proc. R. Soc. London, Ser. A **434**, 101 (1991).
[28]M. Farge, K. Schneider, and N. Kevlahan, ''Non-Gaussianity and coherent vortex simulation for two-dimensional turbulence using an adaptive orthogonal wavelet basis,'' Phys. Fluids **11**, 2187 (1999).
[29]In our previous paper (Ref. 5), the Gaussian curve was erroneously plotted as e^{-x^2}. However, using the form $e^{-x^2/\sqrt{2}}$ matches the area under the curves between the Gaussian and the experimental PDFs. We now use this form in Fig. 8.
[30]A. Arneodo, C. Baudet, F. Belin, B. Castaing, B. Chabaud, R. Chavariia, S. Ciliberto, R. Camussi, F. Chillà, B. Dubrulle, Y. Gagne, B. Hebral, J. Herweijer, M. Marchand, J. Maurer, J. F. Muzy, A. Naert, A. Noullez, J. Peinke, F. Roux, P. Tabeling, W. Vand de Water, and H. Willaime, ''Structure functions in turbulence, in various flow configurations, at Reynolds number between 30 and 5000, using extended self-similarity,'' Europhys. Lett. **34**, 411 (1996).
[31]O. N. Boratav and R. B. Pelz, ''Structures and structure functions in the inertial range of turbulence,'' Phys. Fluids **9**, 1400 (1997).
[32]K. R. Sreenivasan and B. Dhruva, ''Is there scaling at high-Reynolds-number turbulence?'' in *Progress of Theoretical Physics Supplement No. 130*, edited by M. Yamada (AIP, New York, 1998), pp. 103–120.
[33]A. Belmonte, B. Martin, and W. I. Goldburg, ''Experimental study of Taylor's hypothesis in a turbulent soap film,'' Phys. Fluids **12**, 835 (2000).
[34]J.-F. Pinton and R. Labbé, ''Correction to the Taylor hypothesis in swirling flows,'' J. Phys. (France) **4**, 1461 (1994).